Journal of Computational Physics **165,** 407–427 (2000)
doi:10.1006/jcph.2000.6617, available online at http://www.idealibrary.com on IDEAL®

Acceleration of Lattice-BGK Schemes with Grid Refinement

Olga Filippova and Dieter Hänel*

*Institute of Combustion and Gasdynamics, University of Duisburg, D-47048 Duisburg, Germany
E-mail: haenel@vug.uni-duisburg.de

Received July 28, 1999; revised April 27, 2000; published online November 16, 2000

The LBGK method with local grid refinement has been shown to be an efficient and accurate tool for the simulation of incompressible, viscous flows over complex geometries. In the present study, further improvement of this concept is proposed, enabling the use of smaller amount of time steps on refined grids without impairing the spatial or temporal accuracy. This extension of the LBGK method has been proved by analytical and numerical investigations. The gain in computational time was found to be significant.

Key Words: lattice-BGK model; grid refinement.

1. INTRODUCTION

The lattice-Boltzmann method [1, 2] and its recent modification, the lattice-BGK (LBGK) method [3–8], are based on gas-kinetic representations of fluid flow in a strongly reduced "molecular" velocities space. In the simplest LBGK models, the flow is described through the evolution of discrete molecular velocity distribution functions on uniform Cartesian lattices with additional diagonal links. Hydrodynamic variables are computed at the nodes as moments of the discrete distribution functions. The resulting algorithm has been shown to be simple and efficient for computations of incompressible, viscous flows [7, 8, 10, 21] and low Mach number reactive flows [9] over complex boundaries [9, 10].

An essential advantage of the LBGK method is that no discretization of the hydrodynamic equations has to be provided. The macroscopic equations can be deduced after Taylor and Chapman–Enskog expansions of the zero- and first-order moments of the basic equations for distribution functions describing relaxation to the local equilibrium state. The resulting macroscopic equations approximate the Navier–Stokes equations for incompressible flow with second-order accuracy in Knudsen number in space and time in the low-frequency limit. After some modifications of the relaxation scheme in combination with conventional convective-diffusion solvers for equations of temperature and species, the scheme is able

0021-9991/00 $35.00

to solve low-Mach-number flows with strong density gradients caused by heat release in chemical reactions or complex composition of the mixture including species with different molecular weights [9]. The restriction of second-order accuracy in Knudsen number to the low-frequency limit is not very severe because under time-independent external conditions all laminar flows approach to this limit (stationary flows or vortex streets). Therefore, the very simple and stable LBGK scheme with an accuracy of second order in Knudsen number in space and time is suitable for solutions of wide classes of physically relevant problems.

A more severe restriction for the application of the basic LBGK scheme is the identity of the "molecular" lattice and numerical mesh, which makes the scheme macroscopically similar to an uniform Cartesian-grid solver. Nannelli and Succi [11] have extended the original lattice-Boltzmann scheme to handle Cartesian nonuniform grids, borrowing some ideas from the finite volume method. The other approach to extending the LBGK method to curvilinear grids was published by He and Doolen [12, 13] based on the interpolation strategy proposed in [14]. This concept is based on the fixed time step defined by an "underlying" fine LBGK lattice. However, the use of strongly different spacing for the "molecular" lattice and numerical mesh can in general decrease the accuracy of the scheme in the regions of high gradients of macrodynamic variables. To avoid decoupling between "molecular" lattice and numerical mesh, the concept of hierarchical grid refinement was considered [18]. This concept is widely used in conventional CFD methods, e.g., in the method of adaptive mesh refinement (AMR), proposed by Berger and Colella [15] and Quirk [16] and applied to the investigation of detonation waves in [17]. The adaptation of this concept to LBGK schemes was proposed in [18].

In the concept of hierarchical grid refinement, the calculations are based on a coarse grid covering the whole integration domain. In critical region, detected either by adaptation criteria or defined *a priori*, a finer grid is superposed on the basic, coarser grid. The calculation proceeds with large time steps accordingly to the coarse grid, while on the finer grids several time steps are performed to advance to the same time level. In its Cartesian-grid version, this technique is very suitable for lattice BGK models as numerical mesh and "molecular" lattice are not decoupled and therefore the accuracy of the LBGK scheme can be conserved.

In contrast to conventional methods, the employment of locally refined patches in LBGK methods requires more care because the lattice represents the phase space (i.e., the molecular velocity and the local coordinates). The coupling of solutions on the different meshes was solved in [18] through the introduction of different relaxation parameters on the grids with different lattice spacings and rescaling of the nonequilibrium part of distribution functions in transition between different grids.

The local grid refinement strategy allows the resolution of all parts of the flow with approriate accuracy and saves memory and CPU time compared to an uniform grid. However, due to the explicit manner of the LBGK scheme, multiple time steps are necessary on fine grids according to the refinement ratio. For computations of time-dependent reactive flows [9], this feature can be very important, as the use of smaller time steps in the zones of reaction reduces the stiffness of chemical source terms and allows solution of the equations for species and temperature on the same grid as lattice-BGK equations in the simplest explicit manner. But for computations of steady-state and low-frequency incompressible flows the use of n smaller time steps on the fine grid (where n is the spatial refinement factor) can essentially increase the computational time. To remove this drawback the use of smaller amount of time steps in the zones of fine grid is proposed. For time-dependent computations, this is connected with the change of "molecular" speed and reduction of the

number of time steps on the fine grid, but does not impair the temporal accuracy in certain limits. For steady-state computations, the saving of CPU time is much larger, because the same amount of time steps can be chosen on coarse and fine grids, as well. Thus, the proposed acceleration strategy, in combination with grid refinement, improves essentially the performance of lattice BGK method.

The principles of this strategy are outlined in the following and proved by a number of test calculations.

2. BASIC ALGORITHM WITH LOCAL GRID REFINEMENT

The lattice-BGK model is described by the rate of change of a discrete velocity distribution function [3–8]:

$$f_{pi}(t+\delta_t, \mathbf{r}+\mathbf{C}_{pi}\delta_t) = f_{pi}(t,\mathbf{r}) + \omega\left[f_{pi}^{\mathrm{eq}}(t,\mathbf{r}) - f_{pi}(t,\mathbf{r})\right]. \tag{1}$$

The equilibrium distribution function is a discrete analog of the Maxwellian distribution function [5, 6]. For the simulation of incompressible flows with density $\rho_0 = 1$, one can take it in the form [7, 8]:

$$f_{pi}^{\mathrm{eq}} = t_p\left[\frac{P}{\rho_0 C_s^2} + \frac{U_\alpha C_{pi\alpha}}{C_s^2} + \frac{U_\alpha U_\beta}{2C_s^2}\cdot\left(\frac{C_{pi\alpha}C_{pi\beta}}{C_s^2} - \delta_{\alpha\beta}\right)\right] \tag{2}$$

$$P = \rho_0 C_s^2 \sum_{p,i} f_{pi}, \quad \mathbf{U} = \sum_{p,i} f_{pi}\mathbf{C}_{pi}, \tag{3}$$

where $C_s = C/\sqrt{3}$, $C = \delta_x/\delta_t$, δ_x is the lattice spacing and δ_t is the time step. The kinematic viscosity, defined in the frame of the LBGK model [8], depends on the lattice spacing with

$$\nu_0 = \left(\frac{2}{\omega} - 1\right)\frac{\delta_x C}{6}. \tag{4}$$

The essential parameters are the global Mach number M_0 and the Knudsen number ϵ of the flow,

$$M_0 = \frac{U_0}{C}, \quad \epsilon = \frac{\delta_x}{L} = \frac{C\delta_t}{L}, \tag{5}$$

where U_0 is a characteristic velocity and L is a characteristic length of the flow, i.e., the minimal length for this grid on which hydrodynamic variables are essentially changed. The order of this length can differ from one part of the flow to the other.

Considering nondimensional variables

$$u = \frac{U}{C}, \quad c_{pi} = \frac{C_{pi}}{C}, \quad c_s = \frac{C_s}{C} = \frac{1}{\sqrt{3}}, \quad p = \frac{P}{\rho_0 C^2} \tag{6}$$

one can rewrite the expression for the equilibrium distribution function in the LBGK scheme (Eq. 2) as

$$f_{pi}^{\mathrm{eq}} = t_p\left[\frac{p}{c_s^2} + \frac{u_\alpha c_{pi\alpha}}{c_s^2} + \frac{u_\alpha u_\beta}{2c_s^2}\cdot\left(\frac{c_{pi\alpha}c_{pi\beta}}{c_s^2} - \delta_{\alpha\beta}\right)\right], \quad p = c_s^2\sum_{p,i} f_{pi}, \quad \mathbf{u} = \sum_{p,i} f_{pi}\mathbf{c}_{pi}. \tag{7}$$

The nondimensional variables p and $\mathbf{u}$ defined at the nodes of the lattice as zero- and first-order moments of the distribution functions satisfy a system of macrodynamic equations. These equations can be derived from the zeroth- and first-order moments of the expanded LBGK equation, Eq. (1), using a splitting of the discrete distribution function into an equilibrium and nonequilibrium part in the sense of a Chapman–Enskog expansion.

The proof of consistency of these equations in the low-frequency limit with Navier–Stokes equations for incompressible flows can be obtained, for example, from the proof of consistency of LBGK approach for the system of low Mach approximation of Navier–Stokes equations (LMNA) given in [9], in the limiting case of constant density $\rho_{mix} = \rho_0 = 1$. The proof is accompanied by the estimation of asymptotic accuracy of the LBGK scheme. It is of the second order in Knudsen number ϵ both in time and in space if $M_0 \sim \epsilon$.

If the flow is strongly anisotropic, as in the case of high Reynolds number flows, the use of grids with different lattice spacing is necessary to preserve the value of the Knudsen number in the whole computational domain. For the transfer from one grid to the other special care has to be taken to preserve the physical properties of the flow problem. These properties are expressed by the global similarity parameters, as they are

the Reynolds number

$$\mathrm{Re} = \frac{U_0 L_0}{\nu_0} = \frac{6 M_0 L_0}{\delta_x \left(\frac{2}{\omega} - 1\right)} = \frac{6 M_0 L_0 / L}{\epsilon \left(\frac{2}{\omega} - 1\right)} \tag{8}$$

and the Strouhal number

$$\mathrm{Str} = \frac{L_0}{U_0 T_0} = \frac{\delta_t L_0}{\delta_x M_0 T_0} = \frac{\delta_t L_0 / L}{\epsilon M_0 T_0}. \tag{9}$$

Here U_0 is a characteristic flow speed, L_0 is the characteristic length of the flow defined by the geometry, and T_0 is a characteristic time. In the periodical low-frequency flow (as vortex street) T_0 corresponds to the highest hydrodynamic frequency. T_0 differs from the time of a period T_{per} of the oscillating flow which is larger than T_0. The Strouhal number used below in our analysis of macroscopic equations obtained with LBGK scheme is based on T_0. The range of unsteady flows in the low-frequency limit, as mentioned above, is defined by a Strouhal number $\mathrm{Str} = O(1)$, which means that the characteristic time T_0 is of the order of the flow time L_0/U_0.

The basic coarse grid is chosen by such a way that $L = L_0$. Notice that in some cases it requires the redefinition of L_0 and Re. One example is flow around long slender bodies such as airfoils when the angle of attack is not large. In this case, L_0 has to be chosen not as the length of the chord but as the thickness of the airfoil, because this length is on the order of the characteristic length in the wake.

If the grid size is changed, it is required that the Knudsen number ϵ be the same on all grids, where

$$\epsilon = \frac{\delta_x^{\mathrm{c}}}{L_0} = \frac{\delta_x^{\mathrm{f}}}{L}.$$

Here L is the characteristic length of the flow resolved on the fine grid.

The step sizes on coarse and fine grids, δ_x^{c} and δ_x^{f} are connected by the refinement ratio as

$$n = \frac{\delta_x^{\mathrm{c}}}{\delta_x^{\mathrm{f}}} = \frac{L_0}{L}.$$

Assuming that the Mach numbers are the same on coarse and fine grids (the values of Mach number in all overlapping nodes of the both grids are taken from the fine grid) and assuming the same "molecular" speed on the coarse and fine grids $C^{\mathrm{c}} = C^{\mathrm{f}}$, one obtains

$$U_0 = U_0^{\mathrm{c}} = U_0^{\mathrm{f}}.$$

Conservation of the Reynolds number on coarse and fine grids, $\mathrm{Re}^{\mathrm{c}} = Re^{\mathrm{f}}$, is satisfied, if the kinematic viscosities on the both grids are the same, $\nu^{\mathrm{c}} = \nu^{\mathrm{f}}$. From the definition of the kinematic viscosity through the parameters of the LBGK scheme, Eq. (4), the relationship between relaxation parameters on the grids with different lattice spacings is given by [18]

$$\omega^{\mathrm{f}} = \frac{2}{1 + n(2/\omega^{\mathrm{c}} - 1)}. \tag{10}$$

For unsteady low-frequency flows the Strouhal number has to be preserved likewise. This equality,

$$\mathrm{Str}^{\mathrm{c}} = \frac{\delta_t^{\mathrm{c}} L_0}{\epsilon M_0 T_0} = \mathrm{Str}^{\mathrm{f}} = \frac{\delta_t^{\mathrm{f}} L_0/L}{\epsilon M_0 T_0},$$

results in the ratio of time-steps

$$\frac{\delta_t^{\mathrm{c}}}{\delta_t^{\mathrm{f}}} = n.$$

In the following, flows with boundary conditions independent in time will be considered. High-frequency components of solutions dissipate in the transitional stage of computations because no high-frequency disturbances are generated or amplified by the boundary conditions. Then the time advance of LBGK scheme reproduces the low frequency solution

$$\frac{\delta_t^{\mathrm{f}}}{T_0} = (M_0\epsilon)\mathrm{Str}^{\mathrm{c}}/(L_0/L) = \frac{M_0\epsilon\mathrm{Str}^{\mathrm{c}}}{n}. \tag{11}$$

If $M_0 \sim \epsilon \ll 1$ and $n > 1$ then $\delta_t^{\mathrm{f}}/T_0 \sim O(\epsilon^2)$.

3. ACCELERATION OF THE LBGK SCHEME

In the original variant of the local grid refinement technique for the LBGK method [18], the same molecular velocity on the fine and coarse grids is assumed. The calculation proceeds with large time steps according to the coarse grid δ_t^{c}, while on the fine grid n time steps $\delta_t^{\mathrm{f}} = \delta_t^{\mathrm{c}}/n$ are performed to advance to the same time-level, where n is the refinement ratio. To accelerate the algorithm the use of smaller amount of time steps on the fine grid is desired.

The acceleration of the LBGK scheme for time-dependent flows is based on the idea of using different molecular speeds on the fine grid, $C^{\mathrm{f,acc}}$ and on the coarse grid C^{c}. The ratio of the molecular speeds is defined by the parameter of acceleration of the scheme,

$$\Upsilon_0 = \frac{C^{\mathrm{c}}}{C^{\mathrm{f,acc}}} \geq 1.$$

With $\delta_x = C\delta_t$, the time step on the fine grid is

$$\delta_t^{\mathrm{acc}} = \delta_t^{\mathrm{c}} \frac{\Upsilon_0}{n}. \tag{12}$$

The equation (12) shows that for $\Upsilon_0 = 1$ the original refinement is recovered, whereas for $\Upsilon_0 > 1$ the time step is chosen larger.

Despite different molecular velocities, $C^{\mathrm{f,acc}} = C^{\mathrm{c}}/\Upsilon_0$, it is assumed that the local Mach number is conserved on all grid levels. Then the dimensionless velocity (local Mach number) $u^{\mathrm{f,acc}}$ becomes

$$u^{\mathrm{f,acc}} = \frac{U^{\mathrm{f,acc}}}{C^{\mathrm{f,acc}}} = u^{\mathrm{c}} = \frac{U^{\mathrm{c}}}{C^{\mathrm{c}}}.$$

This results in the following rescaling of the dimensional velocity

$$U^{\mathrm{f,acc}} = U^{\mathrm{c}}/\Upsilon_0.$$

From the conservation of Reynolds number, $\mathrm{Re} = U_0 L/\nu$, on all grids follows the relationship between the relaxation parameters of the accelerated scheme on the fine grid $\omega^{\mathrm{f,acc}}$, and on the coarse grid, ω^{c}

$$\omega^{\mathrm{f,acc}} = \frac{2}{1 + n\Upsilon_0(2/\omega^c - 1)}.$$

The expression for the equilibrium distribution function in the accelerated LBGK scheme (more accurately called effective equilibrium distribution function) is prescribed to be

$$f_{pi}^{\mathrm{eq},*} = t_p \left[\frac{p}{c_s^2} + \frac{u_\alpha c_{pi\alpha}}{c_s^2} + \frac{\Upsilon u_\alpha u_\beta}{2c_s^2} \cdot \left(\frac{c_{pi\alpha} c_{pi\,\beta}}{c_s^2} - \delta_{\alpha\beta} \right) \right], \tag{13}$$

where Υ is an additional adjusting parameter (described later).

4. ANALYSIS OF THE ACCELERATED LBGK SCHEME

The proof of consistency of macrodynamic solutions provided by the accelerated LBGK scheme with the solution of Navier–Stokes equations for incompressible flows is based on a consideration of orders of magnitude in the two parameters, the lattice Knudsen number ϵ, and the global Mach number M_0, which are

$$\epsilon = \frac{\delta_x}{L} = \frac{C^{\mathrm{acc}} \delta_t^{\mathrm{acc}}}{L} \ll 1 \quad \text{and} \quad M_0 = \frac{U_0}{C} = \frac{U^{\mathrm{acc}}}{C^{\mathrm{acc}}} \ll 1.$$

On the molecular level, on which the LBGK method is numerically solved, the following nondimensional variables related to C^{acc} and L are introduced:

$$\bar{x} = \frac{x}{L}, \quad \bar{t} = \frac{t C^{\mathrm{acc}}}{L}. \tag{14}$$

The macroscopic variables are related to the following reference quantities:

$$u = \frac{U}{C^{\mathrm{acc}}}, \quad p = \frac{P}{\rho_0 C^{\mathrm{acc}2}}, \quad \nu = \frac{\nu_0}{C^{\mathrm{acc}} L}. \tag{15}$$

The accelerated LBGK scheme reads in nondimensional form

$$f_{pi}(t+\epsilon, \mathbf{r}+\mathbf{c}_{pi}\epsilon) = f_{pi}(t,\mathbf{r}) + \omega^{\mathrm{acc}}\left[f_{pi}^{\mathrm{eq},*}(t,\mathbf{r}) - f_{pi}(t,\mathbf{r})\right] \tag{16}$$

$$\begin{aligned} f_{pi}^{\mathrm{eq},*} &= t_p\left[\frac{p^{\mathrm{acc}}}{c_s^2} + \frac{u_\alpha c_{pi\alpha}}{c_s^2} + \frac{\Upsilon u_\alpha u_\beta}{2c_s^2}\left(\frac{c_{pi\alpha}c_{pi\beta}}{c_s^2} - \delta_{\alpha\beta}\right)\right] \\ p^{\mathrm{acc}} &= c_s^2 \sum_{p,i} f_{pi}, \quad \mathbf{u}_\alpha = \sum_{p,i} f_{pi}\mathbf{c}_{pi\alpha}. \end{aligned} \tag{17}$$

In the following, the bar-superscripts of x and t are skipped for simplicity. Under the assumption of continuous physical space $(t,\mathbf{r})$ in the limit of small ϵ, the LBGK equation, Eq. (16), is expanded in Taylor series with respect to small ϵ,

$$\epsilon\left[\frac{\partial}{\partial t} + c_{pi\alpha}\frac{\partial}{\partial x_\alpha}\right] f_{pi} + \frac{\epsilon^2}{2}\left[\frac{\partial}{\partial t} + c_{pi\alpha}\frac{\partial}{\partial x_\alpha}\right]^2 f_{pi} + \omega^{\mathrm{acc}}\left[f_{pi} - f_{pi}^{\mathrm{eq},*}\right] = O(\epsilon^3). \tag{18}$$

The discrete distribution function can be split into equilibrium and nonequilibrium components as

$$f_{pi} = f_{pi}^{\mathrm{eq},*} + f_{pi}^{\mathrm{neq},*}. \tag{19}$$

The moments of the nonequilibrium distribution function $f_{pi}^{\mathrm{neq},*}$ satisfy:

$$\sum_{p,i} f_{pi}^{\mathrm{neq},*} = 0, \quad \sum_{p,i} f_{pi}^{\mathrm{neq},*} c_{pi\alpha} = 0. \tag{20}$$

Introduction of the expansion Eq. (19) into the Taylor series Eq. (18) and sorting in orders of ϵ results in an expression for the nonequilibrium component $f_{pi}^{\mathrm{neq},*}$

$$f_{pi}^{\mathrm{neq},*}(t,\mathbf{r}) = -\frac{\epsilon}{\omega^{\mathrm{acc}}}\left(\frac{\partial f_{pi}^{\mathrm{eq},*}(t,\mathbf{r})}{\partial t} + \frac{\partial f_{pi}^{\mathrm{eq},*}(t,\mathbf{r})}{\partial x_\alpha} c_{pi\alpha}\right) + O(\epsilon^2). \tag{21}$$

Summation over all discrete velocities in series Eq. (18) with Eq. (19) and Eq. (20) yields the equation of the zeroth moment,

$$\begin{aligned} &\partial_t \sum_{p,i} f_{pi} + \partial_\beta \sum_{p,i} f_{pi} c_{pi\beta} + \frac{1}{2}\epsilon\left(\partial_t\partial_t \sum_{p,i} f_{pi} + 2\partial_t\partial_\beta \sum_{p,i} f_{pi} c_{pi\beta}\right. \\ &\left. + \partial_\beta\partial_\gamma \sum_{p,i} f_{pi}^{\mathrm{eq},*} c_{pi\beta} c_{pi\gamma}\right) = O(\epsilon^2), \end{aligned}$$

and of the first moments by multiplying by $c_{pi\alpha}$,

$$\begin{aligned} &\partial_t \sum_{p,i} f_{pi} c_{pi\alpha} + \partial_\beta \sum_{p,i} f_{pi}^{\mathrm{eq},*} c_{pi\alpha} c_{pi\beta} + \frac{1}{2}\epsilon\left(\partial_t\partial_t \sum_{p,i} f_{pi}^{\mathrm{eq},*} c_{pi\alpha} + 2\partial_\beta\left(1 - \frac{1}{\omega^{\mathrm{acc}}}\right)\right. \\ &\left. \times\, \partial_t \sum_{p,i} f_{pi}^{\mathrm{eq},*} c_{pi\alpha} c_{pi\beta} + \partial_\beta\left(1 - \frac{2}{\omega^{\mathrm{acc}}}\right)\partial_\gamma \sum_{p,i} f_{pi}^{\mathrm{eq},*} c_{pi\alpha} c_{pi\beta} c_{pi\gamma}\right) = O(\epsilon^2). \end{aligned}$$

Using symmetry properties of the lattice,

$$\sum_{p,i} t_p c_{pi\alpha} = 0, \quad \sum_{p,i} t_p c_{pi\alpha} c_{pi\beta} c_{pi\gamma} = 0, \quad \sum_{p,i} t_p c_{pi\alpha} c_{pi\beta} c_{pi\gamma} c_{pi\delta} c_{pi\xi} = 0,$$

$$\sum_{p,i} t_p c_{pi\alpha} c_{pi\beta} = c_s^2 \delta_{\alpha\beta}, \quad \sum_{p,i} t_p c_{pi\alpha} c_{pi\beta} c_{pi\gamma} c_{pi\delta} = c_s^4 (\delta_{\alpha\beta}\delta_{\gamma\delta} + \delta_{\alpha\gamma}\delta_{\beta\delta} + \delta_{\alpha\delta}\delta_{\beta\gamma}),$$

and the expression for the effective equilibrium distribution function, Eq. (17), one can obtain the following nondimensional macrodynamic equations

$$\partial_t \left(p^{\mathrm{acc}}/c_s^2\right) + \partial_\alpha u_\alpha + \frac{1}{2}\epsilon \big(\partial_t \partial_t p^{\mathrm{acc}}/c_s^2 + 2\partial_t \partial_\alpha u_\alpha + \partial_\alpha \partial_\beta (\Upsilon u_\alpha u_\beta + p^{\mathrm{acc}} \delta_{\alpha\beta})\big) = O(\epsilon^2) \tag{22}$$

$$\partial_t u_\alpha + \partial_\beta (\Upsilon u_\alpha u_\beta + p^{\mathrm{acc}} \delta_{\alpha\beta}) = \partial_\beta \nu (\partial_\beta u_\alpha + \partial_\alpha u_\beta + \delta_{\alpha\beta} \partial_\gamma u_\gamma) + \epsilon \left(\frac{1}{2} \partial_t \partial_t u_\alpha + \partial_\beta \left(1 - \frac{1}{\omega^{\mathrm{acc}}}\right) \partial_t (\Upsilon u_\alpha u_\beta + p^{\mathrm{acc}} \delta_{\alpha\beta}) \right) + O(\epsilon^2). \tag{23}$$

Here the nondimensional kinematic viscosity reads as

$$\nu = \frac{c_s^2 \epsilon}{2} \left(\frac{2}{\omega^{\mathrm{acc}}} - 1 \right) = \frac{\epsilon}{6} \left(\frac{2}{\omega^{\mathrm{acc}}} - 1 \right).$$

For $\Upsilon = 1$ the system of equations, Eq. (22) and Eq. (23), results in the continuity equation and the momentum equations of the Navier–Stokes equations for incompressible flow, beside the time derivative of p in the continuity equation and the terms proportional to ϵ in the both equations.

These additional terms are in the order of truncation error in the low-frequency limit. High-frequency components of the solution usually introduced into the LBGK scheme by initial conditions dissipate in the transitional stage of computations if no high-frequency disturbances are generated or amplified by boundary conditions. Thereafter, the time advance of the LBGK scheme reproduces the low-frequency solution only, which corresponds to Strouhal numbers of $\mathrm{Str} \sim O(1)$. This time behavior is typical for laminar vortical flows, for example, for von Karman vortex streets, and was checked by computations.

For verification the system of Equations Eq. (22) and Eq. (23) in molecular scales is transformed to the characteristic scales of the low frequency solutions. The new reference velocity is then a characteristic hydrodynamic velocity U_0 instead of the value of the molecular velocity C^{acc}. The global Mach number $M_0 = U_0/C = U^{\mathrm{acc}}/C^{\mathrm{acc}} \ll 1$ appears then an as additional parameter of magnitude.

The relationship between the nondimensional quantities in Eq. (14) and Eq. (15) and the new dimensionless quantities (with tilde-superscript) is given by:

$$\tilde{x} = \frac{x}{L} = \bar{x}, \quad \delta\tilde{x} = \delta\bar{x} = \epsilon, \quad \tilde{t} = \frac{\bar{t}L}{C^{\mathrm{acc}}T} = \bar{t}\,\mathrm{Str}^{\mathrm{f}} M_0 \Upsilon_0$$

$$\tilde{u} = \frac{uC}{U_0} = \frac{u}{M_0}, \quad \tilde{p} = \frac{P}{\rho_0 U_0^2} = \frac{p^{\mathrm{acc}}}{M_0^2 \Upsilon_0^2}, \quad \frac{1}{\mathrm{Re}^{\mathrm{f}}} = \frac{\nu_0}{U_0 L} = \frac{\bar{\nu}}{M_0 \Upsilon_0}.$$

Notice that here $\mathrm{Str}^{\mathrm{f}}$ and Re^{f} are related to characteristic length on the fine grid L and therefore differ from $\mathrm{Str}^{\mathrm{c}}$, Re^{c} by the factor of n.

Using these transformations with the definition of the time derivative $\partial_{\tilde{t}} = \partial_t/(M_0 \mathrm{Str}^{\mathrm{f}} \Upsilon_0)$, the following equations can be deduced from Eq. (22) and Eq. (23):

$$\mathrm{Str}^{\mathrm{f}} \Upsilon_0^3 M_0^2 \, \partial_{\tilde{t}} \tilde{p}/c_s^2 + \partial_\alpha \tilde{u}_\alpha = O(M_0 \epsilon) \tag{24}$$

$$\begin{aligned} &\mathrm{Str}^{\mathrm{f}} \Upsilon_0 \partial_{\tilde{t}} \tilde{u}_\alpha + \partial_\beta \Upsilon \tilde{u}_\alpha \tilde{u}_\beta + \partial_\alpha \tilde{p} \Upsilon_0^2 \\ &\quad = \partial_\beta \left(\frac{\Upsilon_0}{\mathrm{Re}^{\mathrm{f}}} (\partial_\beta \tilde{u}_\alpha + \partial_\alpha \tilde{u}_\beta + \delta_{\alpha\beta} \partial_\gamma \tilde{u}_\gamma) \right) + O(M_0 \epsilon). \end{aligned} \tag{25}$$

At first the nonaccelerated case $\Upsilon_0 = \Upsilon = 1$ will be considered. Assuming the global Mach number M_0 is on the order of ϵ^a, with $a > 0$ the consistency with continuity and momentum Navier–Stokes equations for incompressible flow is given. Moreover, macrodynamic equations of the LBGK scheme, Eqs. (24) and (25) approximate the solution of Navier–Stokes equations for incompressible flow with asymptotic accuracy of ϵ^2 when $\epsilon \to 0$ and $M_0 \sim \epsilon$.

Usually in numerical simulations with the LBGK scheme, one uses small but finite values of ϵ and M_0 in the order $M_0 \sim \epsilon \sim 0.1$. In this case, the previous asymptotic estimation of accuracy is not sufficient, because in some regions of the flow (as, for example, in the zones of vortex shedding) the space deviations of velocity over the characteristic length can be two orders smaller than the reference value. One way to ensure second order accuracy in ϵ in the whole computational domain is to decrease the global Mach number M_0, which leads inversely to an increase of the computational time and to a loss of the efficiency. The other way is the use of the semiempirical criteria $[\tilde{p}]^{\mathrm{t}} \sim [\tilde{p}]^{\mathrm{s}}$, $[\tilde{u}]^{\mathrm{t}} \sim [\tilde{u}]^{\mathrm{s}}$. Here the notations $[F]^{\mathrm{t}}$, $[F]^{\mathrm{s}}$ are used for the local deviations of variable F on the characteristic time and length accordingly. These estimates are based on the assumption that in the absence of high-frequency components of the solution the local time deviations of the pressure and of the velocity are in the order of their local space deviations. These criteria can be easily checked during the computations. With these estimates one can obtain the following overestimate for $[\tilde{p}]^{\mathrm{s}}$ from the momentum equation $[\tilde{p}]^{\mathrm{s}} \sim [\tilde{u}]^{\mathrm{s}}$, which under the condition $[\tilde{p}]^{\mathrm{t}} \sim [\tilde{p}]^{\mathrm{s}}$ ensures that "wrong" terms in the continuity equation are on the order of $\epsilon^2 [\tilde{u}]^{\mathrm{s}}$ and Eqs. (24) and (25) approximate the continuity and momentum equation of Navier–Stokes equations for incompressible flows with second-order accuracy in ϵ if $M_0 \sim \epsilon$.

Consider now the case of an accelerated scheme where $\Upsilon_0 > 1$. To achieve consistency with the Navier–Stokes equations for incompressible flow, the additional parameter Υ is set equal Υ_0; i.e., $\Upsilon = \Upsilon_0$. By rescaling the pressure in the form

$$\tilde{\tilde{p}} = \tilde{p} \Upsilon_0$$

the parameter Υ_0 can be cancelled in the momentum equation, Eq. (25), such that the physical momentum equation can be achieved with a truncation error of $O(M_0 \epsilon/\Upsilon_0)$, that is $O(\epsilon^2)$ for $M_0 \sim \epsilon$.

In the same way, the continuity equation is satisfied with second-order accuracy in Knudsen number ϵ if

$$\mathrm{Str}^{\mathrm{f}} \Upsilon_0^2 M_0^2 \sim \epsilon^2.$$

Thus, the accelerated scheme is consistent with the Navier–Stokes equations for incompressible flow with second-order accuracy in Knudsen number in space and time if corresponding rescalings are used. A truncation error in time $O(\epsilon^2)$ does not mean second-order

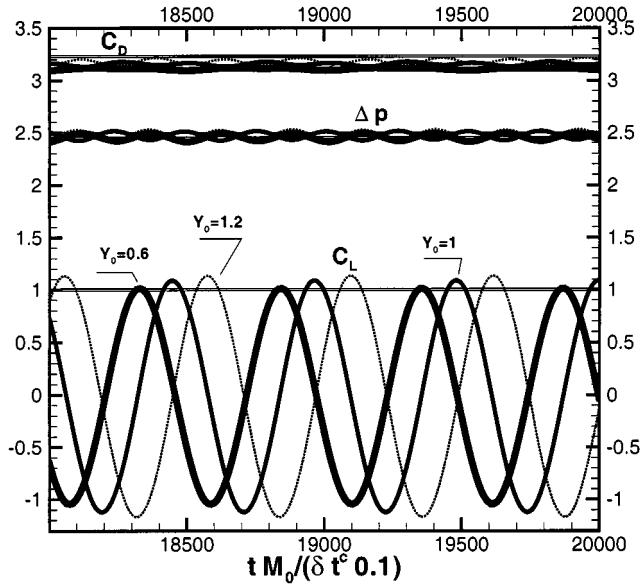

FIG. 1. Temporal development of flow parameters for unsteady flow around a cylinder at Re $= 100$, $M_0 = 0.2$, with $n = 6$ and boundary-fitting conditions on the surface of cylinder. Drag coefficient C_{D}, lift coefficient C_{L}, and pressure difference Δp between the front and end point of cylinder versus non-dimensional time $\frac{t}{\delta^{\mathrm{c}}} \cdot \frac{M_0}{0.1}$ for different Υ_0. Solid thin lines correspond to the case $\Upsilon_0 = 1.2$; solid lines correspond to the case $\Upsilon_0 = 1$; and solid bold lines correspond to the case $\Upsilon_0 = 0.6$. Straight lines are bounds of reference values $C_{\mathrm{D}_{\max}}$, $C_{\mathrm{L}_{\max}}$, $\Delta p(t_0 + T/2)$.

accuracy in time, since

$$\frac{\delta_t}{T_0} = \frac{Str^{\mathrm{c}} M_0 \epsilon \Upsilon_0}{n}.$$

If $M_0 \sim \epsilon$, $\Upsilon_0 = 1$, and $n = 1$, then the time accuracy reduces to first order in δ_t / T_0. Comparison with benchmark results [20] has shown a correct time resolution if $\delta_t / T_0 \sim O(\epsilon^3)$ at least in the vicinity of the body where vortices are appearing. The new acceleration concept offers the possibility of correcting the accuracy by an appropriate combination of the parameters M_0, Υ_0, and n using, for example, the condition

$$\frac{\delta_t}{T_0} = \frac{Str^{\mathrm{c}} M_0 \epsilon \Upsilon_0}{n} \sim \epsilon^3.$$

An example of the influence of this choice is given in Fig. 1.

5. INTERFACE CONDITIONS OF THE ACCELERATED LBGK SCHEME

The compatible interface conditions for local grid refinement are obtained as in [18] from the consideration of an LBGK scheme on two overlapping grids, coarse and fine. On both grids the LBGK scheme provides the macroscopic solution

$$u = u^{\mathrm{NS}}(1 + O(\epsilon^2)), \quad p = p^{\mathrm{NS}}(1 + O(\epsilon^2)),$$

where superscript NS denotes the exact solution of the Navier–Stokes equations for incompressible flow. The nonequilibrium part of the distribution function in the LBGK scheme reads as

$$f_{pi}^{\mathrm{neq}} = -\frac{1}{\omega}\left(\frac{\partial f_{pi}^{\mathrm{eq}}}{\partial t} + \frac{\partial f_{pi}^{\mathrm{eq}}}{\partial x_\alpha} C_{pi\alpha}\right)\delta_t, \tag{26}$$

with second order accuracy in ϵ. For the accelerated LBGK scheme it reads as

$$f_{pi}^{\mathrm{neq},*} = -\frac{1}{\omega^{\mathrm{acc}}}\left(\frac{\partial f_{pi}^{\mathrm{eq},*}}{\partial t} + \frac{\partial f_{pi}^{\mathrm{eq},*}}{\partial x_\alpha} C_{pi\alpha}\right)\delta_t. \tag{27}$$

Introduce the auxiliary postcollision distribution functions

$$f_{pi}^{\mathrm{post}} = f_{pi}^{\mathrm{eq}} + (1-\omega)\cdot f_{pi}^{\mathrm{neq}} \tag{28}$$

for the LBGK schemes with $\Upsilon = 1$ and

$$f_{pi}^{\mathrm{post},*} = f_{pi}^{\mathrm{eq},*} + (1-\omega^{\mathrm{acc}})\cdot f_{pi}^{\mathrm{neq},*} \tag{29}$$

for accelerated LBGK schemes with $\Upsilon > 1$.

For flows with characteristic times T such as $\delta_t/T \sim (M_0 \epsilon \mathrm{Str}^{\mathrm{c}})/n$ and $M_0 \sim \epsilon$, the time derivative of the equilibrium distribution function in Eqs. (26) and (27) becomes of higher order than the spatial derivatives of the equilibrium distribution function. Therefore, Eqs. (28) and (29) can be rewritten with second-order accuracy in Knudsen number ϵ on the coarse grid as

$$f_{pi}^{\mathrm{post,coarse}} = f_{pi}^{\mathrm{eq}} - \frac{1-\omega^c}{\omega^c}\cdot\frac{\partial f_{pi}^{\mathrm{eq}}}{\partial x_\alpha} c_{pi\alpha}\delta_x \tag{30}$$

and for the accelerated LBGK scheme on the fine grid as

$$f_{pi}^{\mathrm{post,fine}} = f_{pi}^{\mathrm{eq},*} - \frac{1-\omega^{\mathrm{f,acc}}}{\omega^{\mathrm{f,acc}}}\cdot\frac{\partial f_{pi}^{\mathrm{eq},*}}{\partial x_\alpha} c_{pi\alpha}\delta_x. \tag{31}$$

Equation (31) can be rewritten with second-order accuracy in Knudsen number ϵ as

$$\begin{aligned} f_{pi}^{\mathrm{post,fine}} = {} & f_{pi}^{\mathrm{eq},*} - \frac{1-\omega^{\mathrm{f,acc}}}{\omega^{\mathrm{f,acc}}}\frac{\partial f_{pi}^{\mathrm{eq}}}{\partial x_\alpha} c_{pi\alpha}\delta_x - \frac{1-\omega^{\mathrm{f,acc}}}{\omega^{\mathrm{f,acc}}} \\ & \cdot \frac{\partial t_p\left((\Upsilon_0-1)p^{\mathrm{NS}} + 0.5(\Upsilon_0-1)u_\gamma^{\mathrm{NS}}u_\delta^{\mathrm{NS}}\left(c_{pi\gamma}c_{pi\delta}/c_s^2 - \delta_{\gamma\delta}\right)\right)}{c_s^2\partial x_\alpha} c_{pi\alpha}\delta_x. \end{aligned} \tag{32}$$

The last term in Eq. (32) can be neglected, and this does not impair the accuracy of the solution as far as its zeroth-order moment is zero and its first-order moment $\sim \delta_x(\partial_\beta p^{\mathrm{NS}}\delta_{\alpha\beta} + u_\alpha^{\mathrm{NS}}u_\beta^{\mathrm{NS}}) \sim [u]^{\mathrm{s}}\epsilon^2$. Up to the coefficient it is the same as introducing the error $\sim\epsilon^3$ in the value of the hydrodynamic velocity. Notice that for $\epsilon \sim 0.1$, the error is lower than ϵ^3 as far as the interface between two grids is usually lying outside of the region of high gradients and therefore the deviation of nondimensional velocity on the characteristic length of the fine grid

in this region is $[u]^{\mathrm{s}} \sim \epsilon L_0/L \sim \epsilon/n$. Together with the overestimate $(1-\omega)/\omega < 0.5$, it provides the error $\sim \epsilon^3/2n$. This becomes important in the region of vortex shedding, where the local value of velocity can be $\sim \epsilon^2$.

Because the values of u^{NS}, p^{NS}, and their spatial derivatives are continuous over the interface between two grids and the relaxation parameter is changed, the following relationships between postcollision distribution functions on the interface are carried out with second-order accuracy in Knudsen number ϵ:

$$\frac{\omega^{\mathrm{f,acc}}}{(1-\omega^{\mathrm{f,acc}})}\left[f_{pi}^{\mathrm{post,fine}} - f_{pi}^{\mathrm{eq},*}\right] = \frac{\omega^{\mathrm{c}}}{(1-\omega^{\mathrm{c}})n}\left[f_{pi}^{\mathrm{post,coarse}} - f_{pi}^{\mathrm{eq,coarse}}\right]. \tag{33}$$

Notice that for the nonaccelerated LBGK schemes and accelerated schemes for steady-state problems using the same amount of time steps on the fine and coarse grid ($\Upsilon = 1$), the expressions of f_{pi}^{eq} are the same on the both grids. Instead of Eq. (33), the following equation is obtained,

$$\frac{\omega^{\mathrm{f}}}{(1-\omega^{\mathrm{f}})}\left[f_{pi}^{\mathrm{post,fine}} - f_{pi}^{\mathrm{eq}}\right] = \frac{\omega^{\mathrm{c}}}{(1-\omega^{\mathrm{c}})n}\left[f_{pi}^{\mathrm{post,coarse}} - f_{pi}^{\mathrm{eq,coarse}}\right], \tag{34}$$

which results in the interface boundary conditions proposed in [18].

The higher order terms appearing from expansion of f_{pi}^{neq}, which are not rescaled correctly by Eqs. (33) and (34), produce an error that does not impair the accuracy of the solution. It can be shown by the following simple arguments. The remained terms of second order in ϵ for the low-frequency limit are proportional to $\sim \delta_x^2 \frac{\partial^2 f_{pi}^{\mathrm{eq}}}{\partial x_\alpha \partial x_\beta} c_{pi\alpha} c_{pi\beta}$ and $\sim \delta_t \frac{\partial f_{pi}^{\mathrm{eq}}}{\omega \partial t}$. Under the assumption that in the low-frequency limit $[p]^{\mathrm{t}} \sim [p]^{\mathrm{s}}$ and $[u]^{\mathrm{t}} \sim [u]^{\mathrm{s}}$ (which can be easily checked during the computations) one can obtain from macrodynamic equations the following overestimate for $[p]^{\mathrm{t}} \sim [p]^{\mathrm{s}} \sim M_0[u]^{\mathrm{s}}$. Taking into account the symmetry properties of the lattice $\sum_{p,i} t_p c_{pi\alpha} c_{pi\beta} c_{pi\gamma} = 0$, $\sum_{p,i} t_p c_{pi\alpha} = 0$, one can conclude that the zeroth-order moment of truncated terms in Eqs. (33) and (34) is of $O(M_0[u]^{\mathrm{s}}\epsilon^2, [u]^{\mathrm{s}}\epsilon^3)$, that is, $\sim \epsilon^4$ for flows with $M_0 \sim \epsilon$, and the first-order moment is of $O([u]^{\mathrm{s}}\epsilon^2)$, that is, ϵ^3 for flows with $M_0 \sim \epsilon$. Actually, it is of the higher order because of the presence of the coefficient $c_s^2(1-\omega)/\omega$, which can be over-estimated as $1/6$.

Although in [18] second-order interpolation on the grid interfaces was proposed, the use of linear interpolation in space and time at the grid interfaces does not change the accuracy of the scheme. Linear interpolation of $f^{\mathrm{eq,coarse}}$ on a link of the coarse grid with size $\delta_x^{\mathrm{c}} = C\delta_t^{\mathrm{c}}$ provides error in the post-collision distribution function of $\sim (\delta_x^{\mathrm{c}})^2 \frac{\partial^2 f_{pi}^{\mathrm{eq}}}{\partial x_\alpha \partial x_\alpha} c_{pi\alpha} c_{pi\alpha}$ and on time-interval $\delta_t^{\mathrm{c}} \sim (\delta_t^{\mathrm{c}})^2 \frac{\partial^2 f_{pi}^{\mathrm{eq}}}{\partial t^2}$. Using the same estimates as before, one can conclude that the common error introduced in the solution on the interface between coarse and fine grids due to the linear interpolation of distribution functions from the neighboring nodes of the coarse grid is consistent with the order of accuracy of the solution on the coarse grid.

6. TEST COMPUTATIONS

6.1. *A Steady-State Problem*

Test calculations are performed for 2-D benchmark problems of incompressible flows defined in [20], which were calculated and compared by many different methods. The test cases describe an incompressible flow around a circular cylinder placed nonsymmetrically

in a long rectangular channel (Re = 20, Re = 100). The stationary 2-D flow case at Reynolds number Re = 20 is used here for validation of the present concept. The computations are performed on a coarse grid (221×43 nodes) with a patch of refinement ratio n around the body covering (26×23) coarse cells. The maximum velocity U at the inlet in units of molecular speed C is equal to 0.1 ($U/C \sim \epsilon$), which results in a relaxation parameter on the coarse grid of $\omega^c = 5/3$. The nonaccelerated LBGK scheme and the accelerated LBGK scheme for steady-state problems ($\Upsilon = 1$) were used in the test calculations. During the first 2000 time steps, the solution is advanced only on the coarse grid with bouncing-back boundary conditions on the surface of the cylinder to accelerate the onset of steady-state flow. Then the development of distribution functions on the fine grid with boundary-fitting conditions on the surface of the cylinder is considered but still without influence to the solution on the coarse grid for 1000 time steps. Finally, the whole exchange of distribution functions between two grids is performed.

In the overlapping nodes of the fine and coarse grids (except the interface coarse-to-fine grid), the values of velocity on the coarse grid are equal to the values of velocity on the fine grid. The convergence criterion is set by

$$\sum_i \frac{\|\mathbf{u}^c(\mathbf{x}_i, t+1) - \mathbf{u}^c(\mathbf{x}_i, t)\|^2}{\|\mathbf{u}^c(\mathbf{x}_i, t+1)\|^2} \le 1 \times 10^{-7}.$$

Results for computations on three successive refined patches are shown in Table I. As seen in Table I, the values of drag coefficients C_D obtained on the finest patch are slightly over the band of reference values [20]. This is connected with the fact that only the patch was successive refined, whereas the surrounding coarse grid was fixed. This results in the fixed error $\sim\epsilon^2$ in the numerical solution.

The Richardson formula

$$p = \log\left(\frac{F_{2h} - F_{4h}}{F_h - F_{2h}}\right) \Big/ \log 2$$

TABLE I

Results for Steady Flow around a Cylinder at Re = 20: Spatial Refinement Factor n, the Number of Time-Steps on the Fine Grid versus One Time-Step on the Coarse Grid N^f, the Values of Drag and Lift Coefficients C_D and C_L, the Pressure Difference Δp between the Front and Back of the Cylinder, the Memory Usage in Mbytes, and the CPU Time in s

n	N^f	C_D	C_L	Δp	Mem	CPU time in s
8	8	5.6118	0.0107	0.1168	19.3	10,938
4	4	5.5392	0.0109	0.1161	8.3	1,720
2	2	5.2321	0.0128	0.1123	5.5	575
Space accuracy		p = 2.08		p = 2.44		
8	1	5.6175	0.0107	0.1169	19.3	2,227
4	1	5.5321	0.0105	0.1160	8.3	765
2	1	5.2286	0.0124	0.1123	5.5	474
Space accuracy		p = 1.83		p = 2.04		
Bandwidth of		5.570	0.0104	0.1172		
reference values [20]		5.590	0.0110	0.1176		

Note. Spatial Accuracy is Presented by the Exponent p.

is used for the proof of accuracy of the scheme with boundary-fitting formulation. It is applied to the values of drag coefficients C_D and to the pressure difference between the front and back points of the cylinder computed on three successive refined patches. The results obtained with nonaccelerated LBGK scheme are shown in the fourth row and with accelerated LBGK scheme in the eighth row. These test results confirm the theoretical estimation of second-order accuracy for the scheme with boundary-fitting formulation [18, 19].

The first observation from Table I is that the spatial accuracy is not impaired by the use of one time-step on the fine grid versus one time-step on the coarse grid. Second, the computational time could essentially be reduced by the lower number of time-steps on the fine grid. Third, the absolute CPU time on an HP9000/C160 workstation is relatively low for such high resolution. Unfortunately, it is rather difficult to compare absolute CPU time with the data available from [20] because the stopping criteria was not defined in conditions of benchmark computations. Considering this part of benchmark computations more as a definition of the order of global CPU time and using also results obtained in our numerical group, we conclude that the CPU times of the accelerated LBGK scheme with local second-order grid refinement compares well with highly developed finite element and finite volume methods.

Notice also that here such a strong side of LBGK schemes as good parallelization was not used. Keeping this in mind, one can conclude that the LBGK scheme with boundary fitting and local grid refinement based on the present acceleration concept is competitive with the best conventional CFD methods and techniques for solution of steady-state problems.

6.2. *A Time-Dependent Problem*

To investigate the properties of the present concept in unsteady flows, the same geometric problem as described before is solved, but at a higher Reynolds number $\mathrm{Re} = 100$. The flow becomes periodically unsteady with development of a vortex street. Definitions and benchmark data are given again in [20].

The computations were performed on a coarse grid (221×43 nodes) with a patch of refinement ratio n around the body covering (23×23) coarse cells. Second-order accurate boundary-fitting conditions on the surface of cylinder were used [18, 19]. In Fig. 1 the computations of drag and lift coefficients and pressure difference on the cylinder are performed for $n = 6$ and a global Mach number of $M_0 = 0.2$. We wish to demonstrate the control of the time accuracy, as discussed in Section 4. The parameter Υ_0 is chosen as $\Upsilon_0 = 1.2, 1, 0.6$.

With the parameter of acceleration $\Upsilon_0 = 1.2$ the maximum value of the lift coefficient differs from its reference value by more than 13%. Decreasing of Υ_0 twice corrects the value of C_L. This demonstrates that the new parameter Υ_0 provides an additional possibility for the local improvement of the time accuracy of LBGK schemes.

Results of the computations with the smaller value of a global Mach number $M_0 = 0.1$ (resulting in a relaxation parameter on the coarse grid $\omega^c = 1.923$), $\Upsilon_0 = 2$, and different refinement ratio n are shown in Table II. We wish to emphasize that the memory usage (and partially CPU time) can be reduced by programming optimizations, which are not the objective of this paper.

As one can see from Table II, the results obtained with second-order boundary-fitting conditions for unsteady problems agree very well with the reference values [20]. Results of computations with the accelerated LBGK scheme ($\Upsilon_0 = 2$) on the patched grid with the refinement ratio $n = 8$ are shown in Fig. 2. The numerical mesh is shown in Fig. 2a; the instantaneous isolines of x-velocity and y-velocity are plotted in Fig. 2b and Fig. 2c. The

TABLE II

Results for Unsteady Flow around a Cylinder at Re = 100: Spatial Refinement Factor n, Parameter of Acceleration of the Scheme Υ_0, Relaxation Parameter on the Fine Grid ω_f, Maximal Values of Drag ($C_{D_{max}}$) and Lift ($C_{L_{max}}$) Coefficients and Pressure Difference $\Delta p(t_0 + T/2)$ between the Front and Back of the Cylinder (t_0 Corresponds to $C_{L_{max}}$), Str Number, Memory Usage in Mbytes, and CPU Time Per Cycle in s for $\Upsilon_0 = 2$ (CPU Time per Cycle in s for $\Upsilon_0 = 1$)

n	Υ_0	ω_f	$C_{D_{max}}$	$C_{L_{max}}$	Δp	Str	Mem	CPU time per cycle in s
6	2	1.351	3.18	1.00	2.49	0.300	18	277 (472)
8	2	1.220	3.23	1.00	2.50	0.300	27	597 (1053)
10	2	1.111	3.246	1.01	2.50	0.300	39	1125 (2008)
Bandwidth of reference values [20]			3.22 3.24	0.99 1.01	2.46 2.5	0.295 0.305		

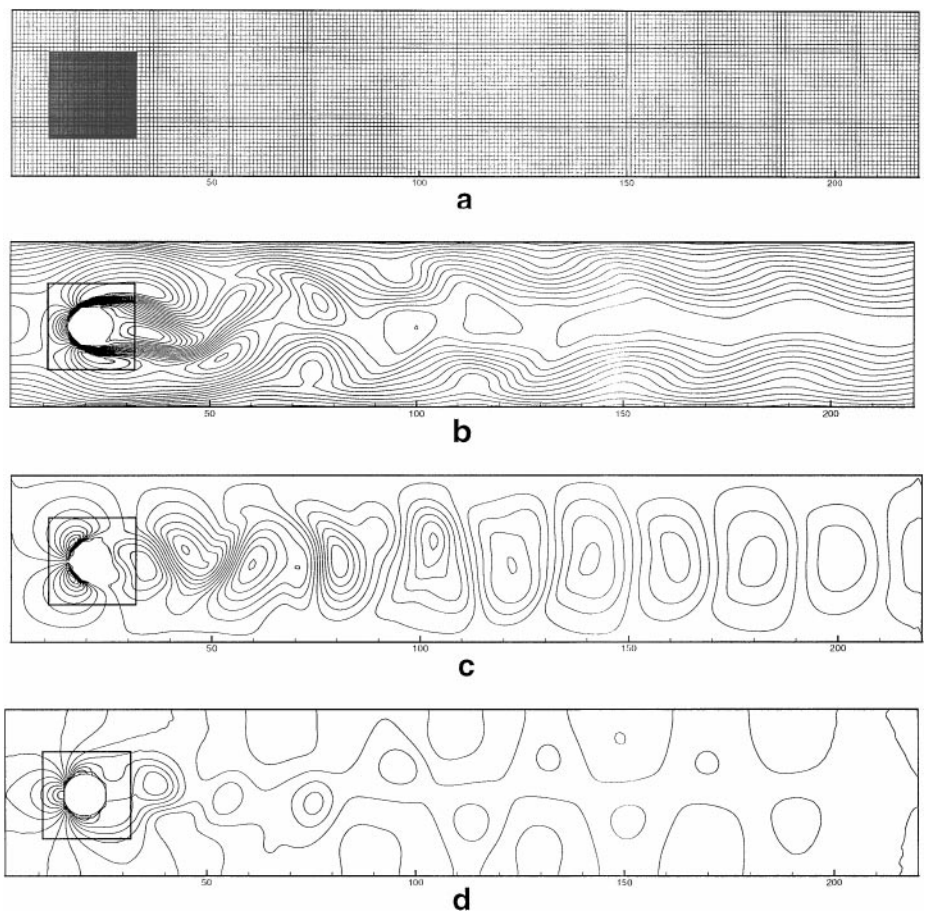

FIG. 2. Unsteady flow around a cylinder at Re = 100 with $n = 8$ and $\Upsilon_0 = 2$: (a) Numerical mesh; (b) instantaneous isolines of x-velocity; (c) instantaneous isolines of y-velocity; (d) instantaneous isobars.

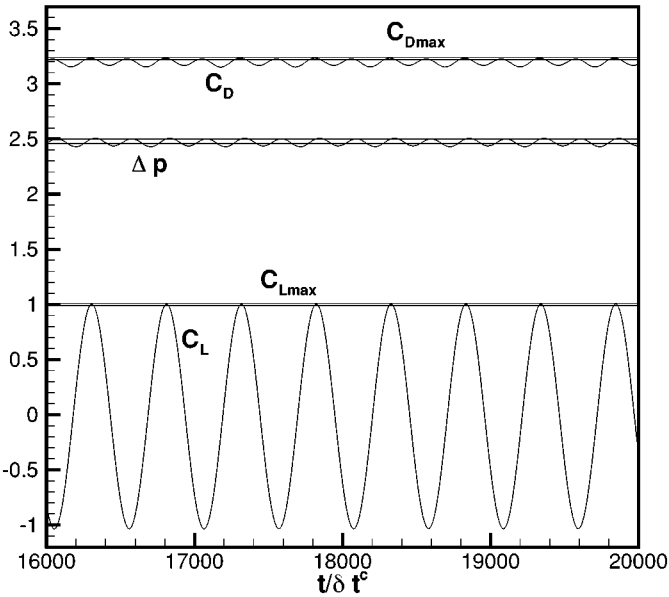

FIG. 3. Temporal development of flow parameters for unsteady flow around a cylinder at $\mathrm{Re} = 100$, $M_0 = 0.1$ with $n = 8$ and $\Upsilon_0 = 2$ and boundary-fitting conditions on the surface of cylinder. Drag coefficient C_D, lift coefficient C_L, and pressure difference Δp between the front and back points of the cylinder versus number of time steps δ_t^c on the coarse grid. Straight lines—bounds of reference values $C_{\mathrm{D}_{\max}}$, $C_{\mathrm{L}_{\max}}$, $\Delta p(t_0 + T/2)$.

instantaneous isobars are presented in Fig. 2d. Figure 3 represents the corresponding drag and lift coefficients and the pressure difference between the front and back points of the cylinder versus the number of coarse time steps. As one can see from Figs. 2 and 3, the reduction of the number of time steps on the fine grid does not influence the accuracy of solution of the finally developed low-frequency time-periodic flow, whereas the computational cost is reduced by a factor close to 2.

A comparison of the performance of the accelerated LBGK model with highly developed finite element and finite volume methods for the Navier–Stokes equations for the same unsteady benchmark problem published in [20] shows the excellent properties of this gas-kinetic solution method. A similar comparative analysis of the results obtained with the LBGK scheme and with finite volume scheme for wake flow past a rectangular cylinder recently published in [21] has also shown excellent agreement. However, the estimation of the comparative performance of both solvers was not the objective of this paper; the LBGK simulations were done on the basic equidistant grid.

7. COMPUTATIONAL EXAMPLE FOR CASCADE FLOW

The proposed scheme using Cartesian-like grids with accurate boundary formulation allows computations of flow around complex geometries in an easy way. Anisotropic flow features are resolved in details by grid refinement, which becomes more efficient by the present acceleration strategy. Thus, this solution method couples the inexpensive grid generation of Cartesian grids with the efficiency of the LBGK method and the high resolution of local grid refinement.

To demonstrate this ability the cascade flow around an airfoil, for the first time considered with multiscale lattice-Boltzmann schemes in steady-state cases in [22], is computed for $\mathrm{Re} = 1000$. The airfoil is described by

$$f(x) = a_1(x - \sqrt{x}) + a_2(x^2 - \sqrt{x}) + a_3(x^3 - \sqrt{x}),$$

where x is normalized to 1 and the coefficients for the upper and lower contours of the airfoil are

$$a_{1\mathrm{low}} = 0.343766, \quad a_{2\mathrm{low}} = -0.02828469, \quad a_{3\mathrm{low}} = -0.1469358$$
$$a_{1\mathrm{up}} = 0.09054341, \quad a_{2\mathrm{up}} = -0.3910232, \quad a_{3\mathrm{up}} = 0.0887612.$$

In an absolute coordinate system $x_0 - y_0$, the integrated domain is a parallelogram ABCD with vertices $A(0, 0)$, $C(0, D_2)$, $B(D_1, D_1 \cdot \mathrm{tg}(\alpha))$, $D(D_1, D_1 \cdot \mathrm{tg}(\alpha) + D_2)$, where $D_2 = 0.99$ is the cascade width, $D_1 = 0.7 + \cos(\alpha) + 0.7$, and $\alpha = 37.5^\circ$. The profile is set with x axis parallel to AB and CD sides just in the middle (at $D_2/2$) and the origin of the x axis is at $x_0 = 0.7$. In the inlet, the velocity is prescribed with an angle $\beta = 53.5^\circ$ with respect to the x_0 axis, which results in an angle of attack on the airfoil of 16°. The outlet pressure is constant, and velocity is extrapolated from the computational domain along the normal to BD. Pressure at the inlet is extrapolated along the normal to AC from the computational domain.

The x-axis of the coarse lattice, covering the whole domain, is directed along the AB side of the parallelogram. The embedded grid with the refinement ratio $n = 4$ is superposed on the basic coarse grid and second-order accurate boundary-fitting conditions [18, 19] are applied on the surface of airfoil. The absolute velocity U at the inlet in units of molecular speed C is equal to 0.1, $(U/C \sim \epsilon)$, which results in the relaxation parameter on the coarse grid $\omega^c = 1.885$. In Fig. 4a, the numerical mesh with embedded grid around the airfoil is shown. Nodes of the Cartesian grid lying outside of the inclined computational domain

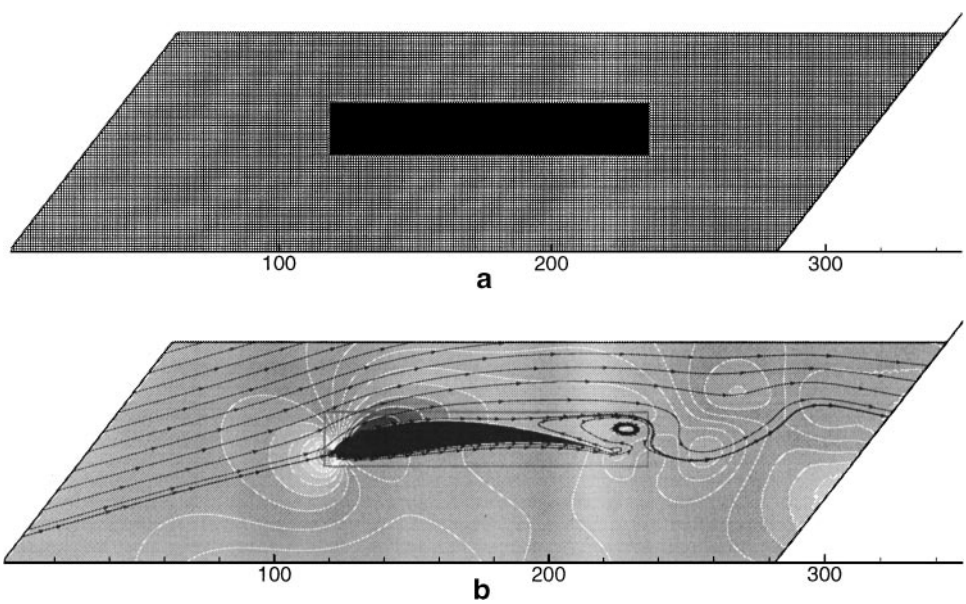

FIG. 4. Unsteady cascade flow around an airfoil at $\mathrm{Re} = 1000$ in a periodical cell: (a) Grid and refined zone with $n = 4$ around an airfoil; (b) isobars and streamlines for $\Upsilon_0 = 2$.

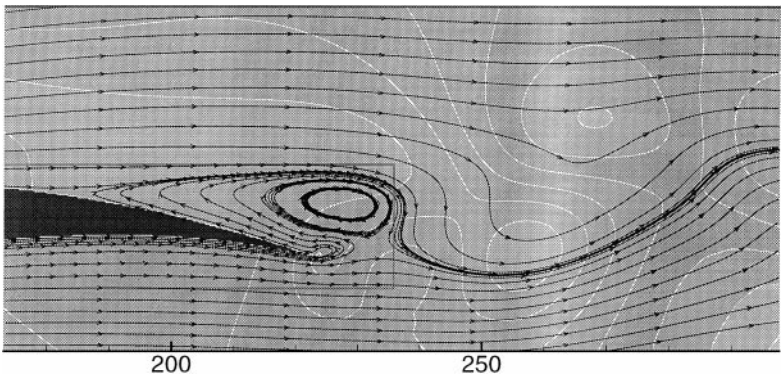

FIG. 5. Unsteady cascade flow around an airfoil at $\mathrm{Re} = 1000$. Isobars and streamlines in the vicinity of the trailing edge at $\Upsilon_0 = 2$ (enlarged part of Fig. 4).

consume 7.6 % of the whole memory usage, but allow the conservation of the simplicity of algorithm. Instantaneous isobars and streamlines of developed low-frequency periodical flow are shown in Fig. 4b. In Fig. 5, the enlarged part of Fig. 4 in the vicinity of the trailing edge is shown. In Fig. 6, the temporal behavior of drag and lift coefficients for $n = 4$ is shown; dotted lines correspond to the nonaccelerated LBGK scheme ($\Upsilon_0 = 1$), solid lines to the accelerated LBGK scheme ($\Upsilon_0 = 2$).

The results for the accelerated and nonaccelerated schemes are shown in Table III. The difference between values obtained with different time-stepping on the fine grid is on the order of accuracy of the solution. The CPU time per cycle obtained with the accelerated LBGK scheme ($\Upsilon_0 = 2$) is better than 1.7 times less than the CPU time per cycle obtained

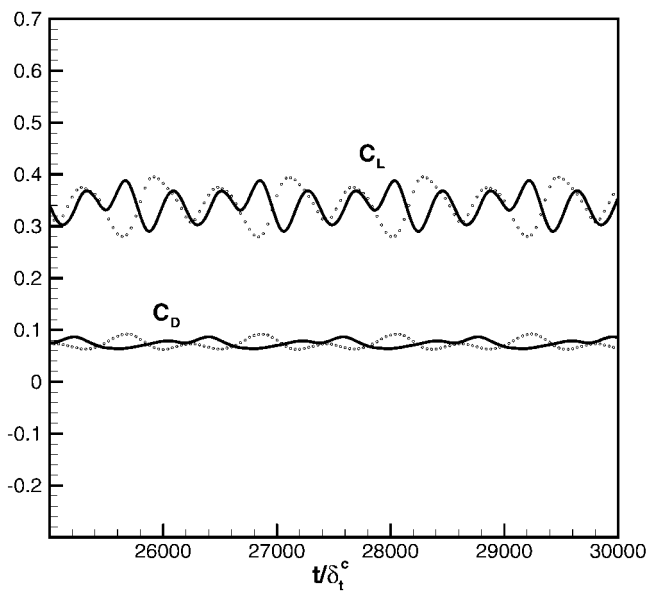

FIG. 6. Unsteady cascade flow around an airfoil at $\mathrm{Re} = 1000$, $n = 4$. Comparison of temporal behaviour of lift (C_L) and drag (C_D) coefficients obtained with nonaccelerated ($\Upsilon_0 = 1$) and accelerated ($\Upsilon_0 = 2$) LBGK schemes (the same case as in Fig. 4 and Fig. 5).

TABLE III

Unsteady Cascade Flow around an Airfoil at Re = 1000: Spatial Refinement Factor n, Parameter of Acceleration of the Scheme Υ_0, Maximal Values of Drag ($C_{D_{max}}$) and Lift ($C_{L_{max}}$) Coefficients, Strouhal Number, Memory Usage in Mbytes, and CPU Time Per Cycle in s

n	Υ_0	$C_{D_{max}}$	$C_{L_{max}}$	Str	Mem.	CPU time per cycle in s
4	1	0.092	0.395	0.860	36.5	2001
4	2	0.081	0.380	0.859	36.5	1162

with the complete variant of grid refinement ($\Upsilon_0 = 1$), and this improvement in CPU time is achieved with zero algorithmic cost. The improvement becomes greater with increased refinement ratio.

The curves of the lift and drag coefficients in Fig. 6 reveal the presence of different frequencies of the periodical flow. The Fourier analysis of the time behavior shows a number of discrete characteristic frequencies (Fig. 7). The frequencies agree very well for both the accelerated and nonaccelerated schemes. However, the amplitudes differ in both cases, so that their superposition in Fig. 6 apparently presents a different behavior.

The sensitivity of time-dependent wake flows behind airfoils to numerical influences, even in the range of the truncation error, was found also in other studies, so for instance, by variations of damping formulations in finite volume methods [23, 24]. Although the order of truncation error remains the same, the change of its value results in change in the relative weight of different frequencies. This change is also displayed with the change of the global Mach number M_0 in the nonaccelerated LBGK scheme.

Notice that in our computations for different time-dependent low-frequency flows, the scheme usually became unstable with Υ_0 more than 2.5. This does not provide severe

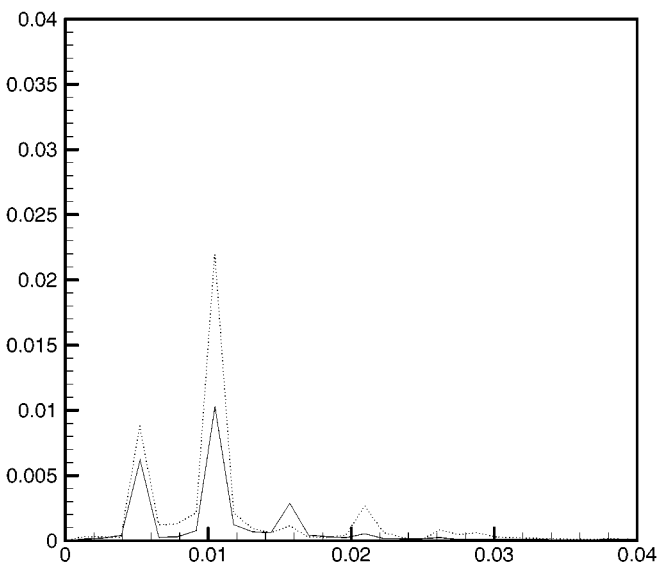

FIG. 7. The absolute values of Fourier coefficients versus frequency for the lift coefficients C_L shown in Fig. 6: solid line—accelerated LBGK scheme; dotted line—nonaccelerated LBGK scheme.

restrictions on the parameter of acceleration of the LBGK scheme inasmuch as with increased Υ_0 for $M_0 \sim \epsilon \sim 0.1$, the "wrong" term in the continuity equation $\sim M_0^2 \Upsilon_0^2$ becomes higher order than ϵ^2, and the accelerated LBGK scheme loses its property as on incompressible solver.

8. CONCLUSIONS

The LBGK method with local grid refinement has been shown to be an efficient and accurate tool for the simulation of incompressible, viscous flows over complex geometries. In the present study, a further improvement of this concept is proposed, which allows the use of smaller number of time-steps on refined grids without impairing spatial or temporal accuracy. This extension of the LBGK method has been proved by analytical and numerical investigations. The gain in computational time was found to be significant. The influence of the global parameters of the scheme on its temporal accuracy is discussed and different possibilities of its local improvement are proposed. Validations by benchmark problems for steady and unsteady flows confirm high accuracy and efficiency, comparable to those of highly developed finite volume and finite element methods for Navier–Stokes equations.

ACKNOWLEDGMENTS

This work has been supported by the DFG (German Research Society). We thank Udo Lantermann for his assistance in the preparation of this paper.

REFERENCES

1. G. McNamara and G. Zanetti, Use of the Boltzmann equation to simulate lattice-gas automata, *Phys. Rev. Lett.* **61**, 2332 (1988).
2. F. Higuera, S. Succi, and R. Benzi, Lattice gas dynamics with enhanced collisions, *Europhys. Lett.* **9**, 345 (1989).
3. S. Chen, H. Chen, D. Martinez, and W. Matthaeus, Lattice Boltzmann model for simulation of magnetohydrodynamics, *Phys. Rev. Lett.* **67**, 3776 (1991).
4. H. Chen, S. Chen, and W. Matthaeus, Recovery of the Navier–Stokes equations through a lattice gas Boltzmann equation method, *Phys. Rev. A* **45**(8), R5339 (1992).
5. Y. H. Qian, D. d'Humieres, and P. Lallemand, Lattice BGK models for Navier–Stokes equation, *Europhys. Lett.* **17**(6), 479 (1992).
6. S. Chen, Z. Wang, X. Shan, and G. D. Doolen, Lattice Boltzmann computational fluid dynamics in three dimensions, *J. Stat. Phys.* **68**, 379 (1992).
7. Q. Zou, S. Hou, S. Chen, and G. Doolen, An improved incompressible lattice Boltzmann model for time-independent flows, *J. Stat. Phys.* **81**, 35 (1995).
8. X. He and L.-S. Luo, Lattice Boltzmann model for the incompressible Navier–Stokes equation, *J. Stat. Phys.* **88**, 927 (1997).
9. O. Filippova and D. Hänel, A novel lattice BGK approach for low Mach number combustion, *J. Comput. Phys.* **158**, 139 (2000).
10. O. Filippova and D. Hänel, Numerical simulation of gas–particle flow in filters by lattice Bhatnagar–Gross–Krook model, in *Advances in Aerosol Filtration*, edited by K. Spurny (CRC Press, Boca Raton, FL, 1998).
11. F. Nannelli and S. Succi, The lattice Boltzmann equation on irregular lattices, *J. Stat. Phys.* **68**(3/4), 401 (1992).
12. X. He and G. Doolen, Lattice Boltzmann method on curvilinear coordinates system: Flow around a circular cylinder, *J. Comput. Phys.* **134**, 306 (1997).

13. X. He and G. Doolen, Lattice Boltzmann method on a curvilinear coordinate system: Vortex shedding behind a circular cylinder, *Phys. Rev. E* **56**(1), 434 (1997).
14. X. He, L.-S. Luo, and M. Dembo, Some progress in lattice Boltzmann method. Part 1. Nonuniform mesh grids, *J. Comput. Phys.* **129**, 357 (1996).
15. M. J. Berger and P. Collela, Local adaptive mesh refinement for shock hydrodynamics, *J. Comput. Phys.* **82**, 67 (1989).
16. J. J. Quirk, *An Adaptive Grid Algorithm for Computational Shock Hydrodynamics*, Ph.D.thesis (Cranfield Inst of Technology, UK, 1991).
17. U. Uphoff, D. Hänel, and P. Roth, A grid refinement study for detonation simulation with detailed chemistry, in *Proc. of 6th Int. Conf. on Num. Combustion, New Orleans, 1996*.
18. O. Filippova and D. Hänel, Grid refinement for lattice-BGK models, *J. Comput. Phys.* **147**, 219 (1998).
19. O. Filippova and D. Hänel, Boundary-fitting and local grid refinement for lattice-BGK models, *Int. J. Mod. Phys. C* **9**(8), 1271 (1998).
20. M. Schäfer and S. Turek, Benchmark Computations of laminar flow around a cylinder, in *Notes in Numerical Fluid Mechanics* (Vieweg Verlag, Braunschweig, 1996), Vol. 52, p. 547.
21. M. Breuer, J. Bernsdorf, T. Zeiser, and F. Durst, Accurate computations of the laminar flow past a square cylinder based on two different methods: Lattice-Boltzmann and finite-volume, *Int. J. Heat Fluid Flow* **21**, 186 (2000).
22. F. Mazzocco, G. Arrighetti, G. Bella, L. Spagnoli, and S. Succi, Multiscale lattice Boltzmann schemes: A preliminary application to axial turbomachine flow simulations, *Int. J. Mod. Phys. C* **11**(2), 233 (2000).
23. K. Dortmann, Computation of viscous unsteady compressible flow about airfoils, in *IC11 NMFD Williamsburg, VA, 1988*.
24. D. Hänel and M. Breuer, On the computation of transonic viscous flows, in *Symposium Transsonicum III, IUTAM Symposium* (Göttingen, Springer-Verlag, 1988), p. 75.